Wind- and tide-induced currents in the Stagnone lagoon (Sicily)

Mauro De Marchis, Giuseppe Ciraolo, Carmelo Nasello & Enrico Napoli

Environmental Fluid Mechanics

ISSN 1567-7419
Volume 12
Number 1

Environ Fluid Mech (2012) 12:81-100
DOI 10.1007/s10652-011-9225-0

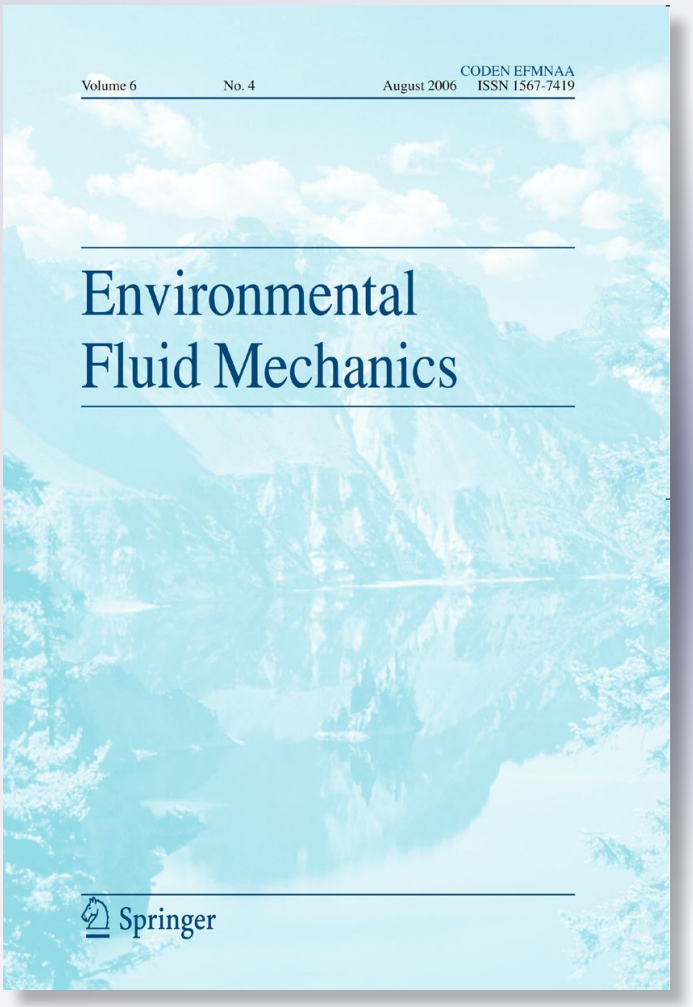

Springer

Environ Fluid Mech (2012) 12:81–100
DOI 10.1007/s10652-011-9225-0

ORIGINAL ARTICLE

Wind- and tide-induced currents in the Stagnone lagoon (Sicily)

Mauro De Marchis · Giuseppe Ciraolo · Carmelo Nasello · Enrico Napoli

Received: 20 September 2010 / Accepted: 12 September 2011 / Published online: 21 October 2011

Abstract The hydrodynamic circulation is analyzed in the coastal lagoon of *Stagnone di Marsala*, a natural reserve located in the north-western part of Sicily, using both experimental measurements and numerical simulations. Field measurements of velocities and water levels, carried out using an ultrasound sensor (3D), are used to validate the numerical model. A 3D finite-volume model is used to solve the Reynolds-averaged momentum and mass balance differential equations on a curvilinear structured grid, employing the k–ε turbulence model for the Reynolds stresses. The numerical analysis allows to identify the relative contribution of the forces affecting the hydrodynamic circulation inside the lagoon. In the simulations only wind and tide forces are considered, neglecting the effects of water density changes. Two different conditions are considered. In the first both the wind stress over the free-surface and the tidal motion are imposed. In the second the wind action is neglected, to separately analyze the tide-induced circulation. The comparison between the two test cases highlights the fundamental role of the wind on the hydrodynamics of the Stagnone lagoon, producing a strong vertical recirculation pattern that is not observed when the flow is driven by tides only.

Keywords Coastal lagoon · Tidal hydrodynamics · Shallow-water · Seiche · Wind-driven flow

1 Introduction

Coastal water bodies are regions of high environmental interest. These areas are characterized by high hydrodynamic spatial and temporal variability, whose analysis has been the object of

M. De Marchis (✉)
Facoltà di Ingegneria, Architettura e delle Scienze Motorie, Università degli Studi di Enna "Kore", Cittadella universitaria, 94100 Enna, Italy
e-mail: mauro.demarchis@unikore.it

G. Ciraolo · C. Nasello · E. Napoli
Dipartimento di Ingegneria Civile, Ambientale ed Aerospaziale, Universita' degli Studi di Palermo, Viale delle Scienze, 90128 Palermo, Italy

several researches mainly focused on the understanding of the physical processes affecting the circulation. The hydrodynamic flow field is driven and/or influenced by several factors, among which the bathymetry, the tidal oscillations, the wind field and the aquatic vegetation distribution. In order to selectively analyze the main forces that drive the hydrodynamic circulation in these regions, several experimental (see Alpar and Yuce [1] and literature therein cited) and numerical studies have been carried out.

Since coastal waters are often characterized by shallowness, two-dimensional shallow-water numerical models have been extensively used to simulate their hydrodynamic behaviour. Suursaar et al. [26], employing a 2D hydrodynamic model to analyze the circulation of a sub-basin of the Baltic Sea, observed that the wind velocity over the free-surface has strong impact on the circulation and that the modelling accuracy can be improved by increasing the resolution of the wind input data. Following the same line, Kramer and Jozsa [13] used a 2D shallow-water equation model, to analyze the wind-induced steady-state circulation in the lake Neusiedl (situated on the border of Hungary and Austria) and the unsteady currents in the Fertőrákos Bay (in the Hungarian part of the lake). The authors mainly focused on the application of the quadtree-based adaptive mesh algorithm [4], showing that the method is robust and flexible for use in natural lakes characterized by complex morphology. Later, the efficiency of the solution-adaptive algorithm was verified by Kramer and Jozsa [14], while considering 2D modelling of wind-induced currents in shallow-waters characterized by variable bed topography and aquatic vegetation.

Babu et al. [2] demonstrated a seasonal wind-dependence of the flow in the Gulf of Kachchh (India), showing that the wind plays a significant role in determining the currents. Ferrarin and Umgiesser [8], using a 2D finite element model resolving the vertically integrated shallow-water equations, analyzed the contemporary effect of both wind and tide forces on the hydrodynamic in the Cabras lagoon (Italy). They also observed that the wind is the main force responsible for the circulation, while the tides determine the discharges through the inlet mouth of the lagoon and modulate the circulation driven by the wind. A large influence of the tide was found by Niedda and Greppi [21], who investigated the different mechanisms that affect the circulation in a small lagoon of the Mediterranean sea. They carried out numerical simulations with a two-dimensional horizontal model and compared the results with experimental observations. Their analysis points out that the balance of tidal, atmospheric and seiche forces is responsible for the hydrodynamic behaviour in the considered lagoon.

Even stronger impact of tidal effects was observed by Iglesias et al. [11] that analyzed the effect of wind and tide on the circulation in the coastal embayment of Ria de Muros (Spain). Their analysis leads to the conclusion that the tide is the main force driving the circulation. They also concluded that the hydrodynamic pattern is characterized by typically 3D features, thus suggesting the need for 3D numerical models.

The same argument had been already suggested in 2002 by Balas and Ozhan [3], who carried out 3D numerical simulations in the Göksu Lagoon (Turkey), where the current was found to be mainly driven by the wind force. The authors pointed out that, even if the water depth is quite shallow, some recirculation phenomena in the vertical plane can be found, thus motivating the use of 3D numerical models. Three-dimensional modelling was employed too by Marinov et al. [18] to analyze a coastal lagoon of the Adriatic Sea, and by Grifoll et al. [10], who studied the hydrodynamic condition within the Bilbao Harbour (Spain). The analysis of Grifoll et al. [10] shows that the circulation pattern in the harbour is affected by tides, wind and the presence of freshwater as well. The need of accounting for both wind and tide forces in coastal waters was also demonstrated by MacCready et al. [17] in their study of the Columbia river estuary. Recently, Ferrarin et al. [9] studied the hydraulic regime in

the Lagoons of Marano and Grado (Italy) using a finite element model to resolve the shallow-water equations. The variability of salinity, water temperature and hydraulic circulation was analyzed in order to derive a hydraulic regime-based zonation scheme. The three-dimensional models discussed so far employed the RANS approach to obtain the turbulence closure. A more refined analysis of the turbulence has been performed by Roman et al. [24], who used the Large Eddy Simulation technique with directional eddy viscosity to account for the large anisotropy of the resolved scales.

The literature above analyzed shows that the relative effect of wind and tides on coastal shallow water hydrodynamics can significantly change in different topographic and forcing conditions and that in several cases three-dimensional analyses can improve the overall accuracy of the results.

The main scope of this research is to contribute to the understanding of the effect of the different forces driving the hydrodynamics and the circulation patterns in shallow coastal lagoons using non hydrostatic 3D numerical modelling. A three-dimensional description of the flow field could have been obtained using hydrostatic 3D models as well [6]. Nevertheless, the hydrostatic approximation on the pressure distribution can largely affect the time evolution of the velocity field, particularly in flows driven by unsteady winds and tidal forces and/or developing over relatively steep bathymetry gradients or around obstacles. In all these cases vertical accelerations of the fluid cannot be neglected and thus fully-3D non-hydrostatic models must be used even for very shallow waters.

The Stagnone di Marsala, located in the north-western part of Sicily, is analyzed through both experimental observations and numerical simulations. After validating the numerical results through their comparison with measured data, the attention is focused on the relative contribution of the wind flow field acting on the free-surface and the tidal oscillations.

The paper is organized as follow: Sect. 2 describes the study area, the collected experimental data and the numerical model. The validation of the hydrodynamic model is addressed in Sect. 3 and the discussion of the results obtained is reported in Sect. 4. Conclusions are drawn in Sect. 5.

2 Materials and methods

2.1 Study area

The lagoon of Stagnone, located in front of the Marsala town (Sicily), is an important natural reserve from both the ecological and economical points of view. The lagoon is about 11 km long (in the north-south direction) and about 2.5 km width (in the east-west direction). It is enclosed between the Sicilian coast and the island *Isola Grande*. The lagoon, shown in Fig. 1, is connected to the Mediterranean sea through the northern and southern mouths. The mouth located in the northern part of the basin is about 400 m wide with an average depth of only 0.3–0.4 m. The water shallowness thus highly limits the volume exchanges between the northern part of the lagoon and the open sea. With the aim to increase the local flushing capability, a 15 m wide and 1.0 m deep artificial channel was dredged in the past, parallel to the west coast of the northern mouth (see the satellite map in Fig. 1). On the other side, the southern inlet, characterized by a wide mouth of about 2.9 km and a depth spanning between 1.0 and 1.50 m, ensures the mass exchange between the open sea and the lagoon, allowing for the water mixing.

The mean water depth in the basin is about 1.0 m, with minimum and maximum values approximatively of 0.20 and 3.00 m, respectively. In Fig. 1 the bathymetry of the lagoon

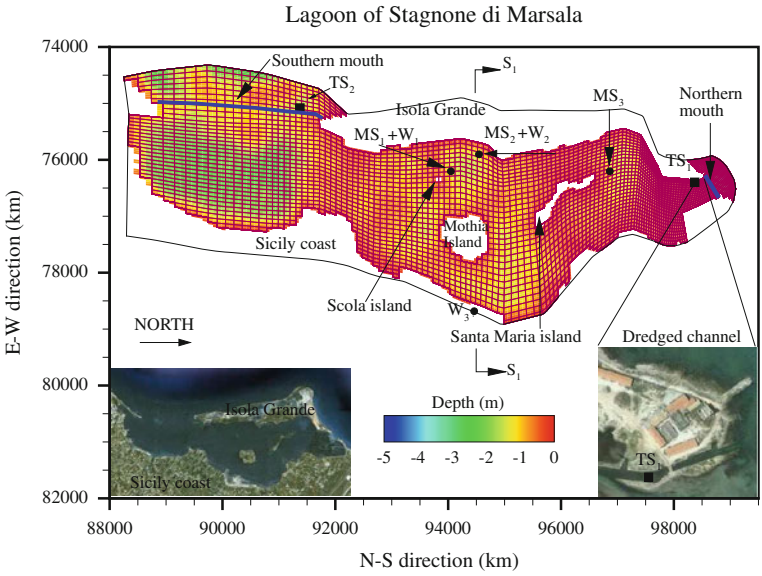

Fig. 1 Stagnone di Marsala Lagoon. The bathymetry and the grid of the numerical simulation are superimposed. Measurement points of the water level near the lagoon mouths (TS_1 and TS_2) and inside the lagoon (MS_1 and MS_2), of the wind velocity (W_1, W_2 and W_3) and of the current velocity (MS_1). The number of cells in the figure has been reduced by a factor of four to improve clarity

is also shown. Two small islands, *Mothia* and *Santa Maria*, are located in the central and northern parts of the lagoon. A very small island, called *Scola*, is also present in the central region of the lagoon, besides an ancient submerged road connecting the Mothia island with the Sicilian coast in the south-north direction.

The hydrodynamic circulation inside the lagoon is predominantly driven by tidal and wind forces, since no freshwater is discharged, thus making very low the density changes; the episodic watershed runoff, mostly occurring during the rainfall season, are negligible as well. The sandy bottom is partially covered by two main species of seagrass. The northern part is characterized by the presence of *Cymodocea nodosa*, while the central-southern region is covered by *Posidonia oceanica*, sometimes emerging during low tide.

The great naturalistic interest of the lagoon in the Mediterranean sea is mainly due to the presence of typical vegetal and animal species. The lagoon ecosystem requires a strong water exchange rate to survive, but, unfortunately, during last decades the lagoon connection with the open sea became insufficient due to bottom uplift and strong sedimentation near the northern mouth. The particular topography and interaction of driving forces make the lagoon hydrodynamics highly complex, thus motivating the use of accurate 3D modelling.

2.2 The monitoring data

In order to corroborate the proposed numerical model, field measurements were carried out. Both hydrodynamic variables (water levels and current velocities) and meteorological data (wind velocity components and direction) were acquired. Specifically, wind velocities and water levels close to the lagoon mouths were used as input data to force the model, while velocities and water levels inside the lagoon were employed to verify the numerical model results.

The wind speed and direction were measured in correspondence of the W_1, W_2 and W_3 points shown in Fig. 1. In the measurement station W_1 a 3D Sonic Anemometer was installed to measure the wind speed at high frequency (25 Hz), while at the platform W_2 a wind station (Aanderaa instruments) was located to record wind intensity and direction every minute (with values smoothed in time applying a 15 minutes average). The meteorological gauge W_3 was located over a building at the height of about 10 m above the ground, while the gauges W_1 and W_2 were located at the height of 3 m. Wind speed and direction were measured every 5 seconds and the mean values were recorded for each sector every 15 minutes. As it will be discussed in Sect. 3, in the numerical simulations the wind measurements at the W_2 station have been used.

The water elevation at the northern mouth (station TS_1, Fig. 1) was registered using a float-operated Shaft Encoder (Ott Thalimedes), located in a box connected with the dredged channel of the mouth. The sea level was measured every one minute, while the mean value was recorded every 5 minutes. A second measure of the free-surface level near the southern mouth (station TS_2, Fig. 1) was obtained through a pressure sensor data logger (Valeport 808 EM).

In order to check the model accuracy, the water velocity was measured in a station located in the central region of the lagoon (MS_1 in Fig. 1), where the 3D Acoustic-Doppler Velocimeter (ADV) ultrasound current meter was deployed. The data were acquired with a sampling rate of 25 Hz. The accuracy of the used ADV Ultra sound current meter was within 0.25 ± 2.5 mm/s. In the measurement stations MS_2 and MS_3 the water depth above the free-surface through a pressure sensor was registered.

The field campaign was carried out from the 5th to the 9th of July 2006.

2.3 Mathematical and numerical model

The incompressible Reynolds Averaged Navier-Stokes and continuity equations, in the summation convention formulation, read:

$$\frac{\partial u_i}{\partial t} + \frac{\partial u_i u_j}{\partial x_j} - \nu \frac{\partial^2 u_i}{\partial x_j \partial x_j} + \frac{1}{\rho}\frac{\partial p}{\partial x_i} + \frac{1}{\rho}\frac{\partial \tau_{ij}}{\partial x_j} + g\delta_{ij} + f_i = 0 \quad i, j = 1, \ldots, 3 \tag{1}$$

$$\frac{\partial u_j}{\partial x_j} = 0 \quad j = 1, \ldots, 3 \tag{2}$$

where t is the time, x_i the i-th axis (with the axes x_1, x_2 and x_3 aligned with the east-west, north-south and vertical directions respectively), u_i the i-th component of the Reynolds averaged velocity, ρ the water density, p the Reynolds averaged pressure, g the gravity acceleration, ν the kinematic viscosity, δ_{ij} the Kronecker delta, f_i the i-th component of the Coriolis acceleration and $\tau_{ij} = \rho\overline{u_i' u_j'}$ the Reynolds stresses, being u_i' the fluctuating velocity and indicating $\bar{\cdot}$ the Reynolds averaging. The pressure p can be splitted into the sum of the hydrostatic part, dependent on the free-surface elevation, and the excess ρq over hydrostatic pressure:

$$p = \gamma[(z_B + h) - x_3] + \rho q \tag{3}$$

where $z_B(x_1, x_2)$ is the bed elevation from an horizontal plane of reference and $h(x_1, x_2)$ is the water depth (see Fig. 2).

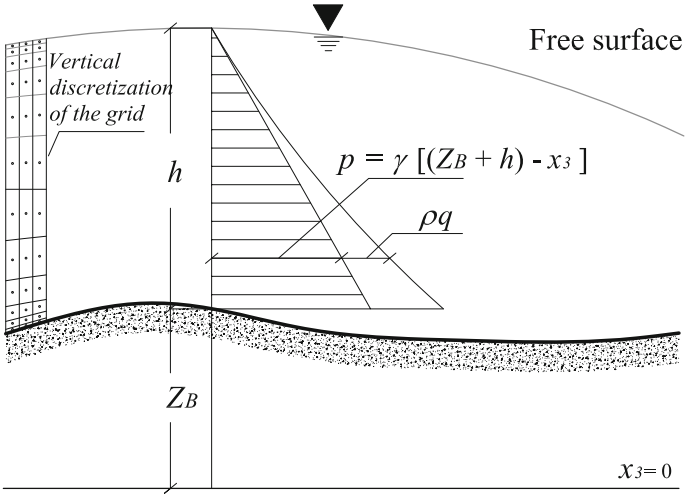

Fig. 2 Hydrostatic and non-hydrostatic pressures and geometrical definitions

Introducing Eq. 3 into Eq. 1, the Reynolds Averaged Navier-Stokes equations can be rewritten as:

$$\frac{\partial u_i}{\partial t} + \frac{\partial u_i u_j}{\partial x_j} - \nu \frac{\partial^2 u_i}{\partial x_j \partial x_j} + \frac{\partial q}{\partial x_i} + \frac{1}{\rho}\frac{\partial \tau_{ij}}{\partial x_j} + f_i + g\frac{\partial (z_B + h)}{\partial x_i} = 0 \quad i, j = 1, \ldots, 3 \tag{4}$$

The last term is null for $i = 3$, due to the independence of z_B and h from x_3.

Due to the high grid anisotropy, with horizontal spacing much larger than the vertical one, the turbulence closure is achieved by using a non-isotropic eddy viscosity coefficient, as it is customary in oceanographic applications [24,25]. Here the non-isotropic coefficient is obtained through the sum of an isotropic coefficient ν_t, calculated using the k-ε model in the standard formulation of Launder and Spalding [15], and an horizontal eddy viscosity coefficient $\nu_{h,t}$, acting on the horizontal terms only, calculated through the Smagorinsky model (it is worthwhile to point out that, although the Smagorinsky model is mainly used in the framework of the Large Eddy Simulation technique, here the RANS approach is employed). The turbulence terms in the Eq. 4 are thus expressed as

$$\begin{aligned}\frac{1}{\rho}\frac{\partial \tau_{ij}}{\partial x_j} = &-\frac{\partial}{\partial x_j}\left[\nu_t\left(\frac{\partial u_i}{\partial x_j} + \frac{\partial u_j}{\partial x_i}\right)\right] \\ &-(1-\delta_{i3})(1-\delta_{j3})\frac{\partial}{\partial x_j}\left[\nu_{h,t}\left(\frac{\partial u_i}{\partial x_j} + \frac{\partial u_j}{\partial x_i}\right)\right] + \frac{2}{3}\delta_{ij}k\end{aligned} \tag{5}$$

where k is the turbulent kinetic energy (TKE) per unit mass and the product $(1-\delta_{i3})(1-\delta_{j3})$ is different from zero for $i = 1, 2$ and $j = 1, 2$ (the horizontal terms).

The isotropic eddy viscosity ν_t is obtained as:

$$\nu_t = c_\mu \frac{k^2}{\varepsilon} \tag{6}$$

where c_μ is a closure parameter and ε the dissipation rate of the TKE. The time and space distribution of k and ε are obtained through:

$$\frac{\partial k}{\partial t} + \frac{\partial u_i k}{\partial x_j} = \frac{\partial}{\partial x_j}\left(\frac{\nu_t}{\sigma_k}\frac{\partial k}{\partial x_j}\right) + P - \varepsilon \tag{7}$$

$$\frac{\partial \varepsilon}{\partial t} + \frac{\partial u_i \varepsilon}{\partial x_j} = \frac{\partial}{\partial x_j}\left(\frac{\nu_t}{\sigma_\varepsilon}\frac{\partial \varepsilon}{\partial x_j}\right) + (c_{\varepsilon 1} P - c_{\varepsilon 2}\varepsilon)\frac{\varepsilon}{k} \tag{8}$$

where P is the production of the TKE:

$$P = -\overline{u_i' u_j'}\frac{\partial u_i}{\partial x_j} \tag{9}$$

The standard values of the model coefficients are used: $c_\mu = 0.09$, $c_{\varepsilon 1} = 1.44$, $c_{\varepsilon 2} = 1.92$, $\sigma_k = 1.0$ and $\sigma_\varepsilon = 1.3$.

The horizontal eddy viscosity is obtained as

$$\nu_S = (C\Delta)^2 \|S\|$$

where Δ is a length scale of the horizontal grid spacing (obtained as the square-root of the area of the cell projection onto an horizontal plane), C is a closure coefficient (to which the value of 0.2 was assigned) and $\|S\|$ is a norma of the horizontal Reynolds averaged strain-rate tensor S_{mn}:

$$\|S\| = \sqrt{2 S_{mn} S_{mn}} \quad \text{with} \quad S_{mn} = \frac{1}{2}\left(\frac{\partial u_m}{\partial x_n} + \frac{\partial u_n}{\partial x_m}\right) \quad \text{m, n} = 1, 2$$

The free-surface elevation is advanced in time according to the kinematic boundary condition:

$$\frac{\partial h}{\partial t} + u_{1,s}\frac{\partial (z_B + h)}{\partial x_1} + u_{2,s}\frac{\partial (z_B + h)}{\partial x_2} - u_{3,s} = 0 \tag{10}$$

where $u_{i,s}$ are the surface velocity components.

The above equations are numerically solved using the 3D numerical model PANORMUS (parallel numerical open-source model for unsteady flow simulation) developed at the Department of Hydraulic and Environmental Application Engineering (DIIAA) of the University of Palermo [19]. The employed numerical scheme is second-order accurate both in time and space. The algorithm used for the time advancement of the solution is semi-implicit in the vertical direction. Specifically, the vertical diffusive and turbulent terms are discretized using the Crank-Nicolson implicit method, while the Adams-Bashforth explicit scheme is employed for the remaining terms. An implicit discretization is used for the vertical viscous and turbulent terms since the stability restriction arising from these terms result to be much more severe than that related to the horizontal corresponding ones. The CFL condition too is more restrictive in the vertical direction than in the horizontal one, despite the much higher horizontal velocities, due to the much finer vertical grid resolution (by two or three orders of magnitude). The time step used in the computation is set to 0.5 s to satisfy the stability limits during the whole simulation.

The pressure–velocity decoupling, typical of incompressible fluids, is overcome using a fractional-step method [22]. The discretized momentum equations are first solved assuming hydrostatic pressure distribution (*predictor-step*), to obtain the *predictor-step velocity* u_i^*:

$$\frac{u_i^* - u_i^n}{\Delta t} + \frac{3}{2}\left(C_i^n + D_{h,i}^n + T_{h,i}^n + R_i^n + G_i^n\right) - \frac{1}{2}\left(C_i^{n-1} + D_{h,i}^{n-1} + T_{h,i}^{n-1} + R_i^{n-1} + G_i^{n-1}\right) + \frac{1}{2}\left(D_{v,i}^* + T_{v,i}^* + D_{v,i}^n + T_{v,i}^n\right) = 0 \quad i = 1, \ldots, 3 \tag{11}$$

where C_i, $D_{h,i}$, $D_{v,i}$, $T_{h,i}$, $T_{v,i}$, R_i and G_i indicate the discretized forms of the convective, horizontal diffusion, vertical diffusion, horizontal turbulent diffusion, vertical turbulent diffusion, Coriolis and mass force terms, respectively.

Since the predictor-step velocity field u_i^* is not divergence-free, the Poisson-like equation

$$\frac{\partial^2 \Psi}{\partial x_j \partial x_j} = -\frac{\partial u_j^*}{\partial x_j} \quad i = j, \ldots, 3 \tag{12}$$

is then solved at each time step to obtain the potential Ψ of an irrotational velocity field $u_{i,c} = \partial\Psi/\partial x_i$, having opposite divergence to the predictor-step velocity field, to be added to u_i^* (*corrector-step*).

The divergence-free updated velocity field u_i^{n+1} is thus obtained as the sum $u_i^{n+1} = u_i^* + u_{i,c}$.

The free-surface elevation is updated at each time step according to Eq. 10.

In the vertical direction a non-uniform discretization is used, with a refinement close to the bottom and the free-surface. The level of refinement is set tuning the parameter α in the hyperbolic function:

$$d_k = 0.5h \cdot [tanh(\alpha(r-1)) + (tanh(-\alpha) + 1)(r-1) + 1] \tag{13}$$

where d_k is the distance of the k-th node from the bottom, n is the number of grid cells in the vertical direction, h is the water depth and $r = 2(k-1)/n$. The parameter α controlling the node clustering is locally tuned to obtain a vertical resolution not higher than 0.05 m in the top cell (resulting in a null value of the parameter and an uniform vertical discretization where the water depth is lower than $0.05\,n$ m).

Details on the numerical discretization and extensive validation of PANORMUS model against laboratory and field experiments in several different conditions can be found in Cioffi et al. [6], De Marchis and Napoli [7], Lipari and Napoli [16] and Napoli et al. [20].

3 Model validation

In order to validate the model a comparison between simulated and observed data has been performed. The validation period corresponds with the period of field measurements (5th to 9th July 2006), as discussed in Sect. 2.2. In the numerical simulations the computational domain has been discretized using $84 \times 293 \times 12$ cells in the east-west, north-south and vertical directions, respectively. The horizontal projection of the computational grid is plotted in Fig. 1. Due to the geometrical complexity of the domain and the presence of three islands, a curvilinear boundary-fitted computational grid was used, where the cells corresponding to land areas (see Fig. 1) have been excluded from the computation. Boundary conditions identical to those used at the lateral solid walls were used at the *internal* boundaries created by the blanked-out cells. In order to make simpler the discretization, the coast-line was somewhat regularized, using a step-like pattern. More accurate description of the coast-line could have

been obtained using techniques as the Immersed Boundary Method, whose application to curvilinear grids was recently proposed by Roman et al. [23]. Nevertheless, since the velocities close to the lateral boundary were quite low due to the very limited flow depth (in most cases significantly lower than the average values), the increase in the computational effort required by the use of these methods would not have been justified.

In order to reproduce the field conditions, the numerical simulation has been performed taking into account both tidal and wind forces. The water level oscillations measured in the northern and southern mouths, indicated in Fig. 1 with TS_1 and TS_2, respectively, plotted in Fig. 3a, have been filtered applying the low-pass Butterworth filter, thus removing the seiche oscillations from the measured signal (Fig. 3b). The filtered oscillations have been imposed at the open boundaries, that have been placed some hundreds of meters far from the mouths toward the open sea, where the seiche effects are not present, as shown in Fig. 1.

As discussed in Sect. 2.2, the wind speed velocity has been measured in three different stations. Two stations are located inside the lagoon (identified as W_1 and W_2 in Fig. 1), while the third one (W_3) on the land. In Fig. 3c, d the measured east-west and north-south wind velocity components are plotted. The general trend of the time dependent wind velocity in the three stations is quite similar, suggesting that a constant spatial distribution can be used in the simulation (although some differences can be seen in the land wind with respect to the one blowing over the water). In the simulations the wind field in the W_2 station has been thus used.

The wind speed produces a wind shear stress over the free-surface, which is calculated as $\tau_s = \rho_{air} u_*^2$, where ρ_{air} is the air density and u_* is the air friction velocity at the free-surface. This friction velocity can be related to the wind speed W_{10} at the standard height of 10 m and to the wind drag coefficient C_{10} through the formula: $C_{10} = (u_*/W_{10})^2$. The wind drag coefficient is calculated by the widely employed Wu's formula [27]: $C_{10} = (0,8 + 0,65 W_{10}) \cdot 10^{-3}$. Since the wind in W_2 was measured at the height of 3 m above the water level, the logarithmic velocity profile has been used to obtain the 10 m height velocity W_{10}. The obtained shear stress τ_s was then applied over the free-surface in the wind direction.

The distribution of seagrass on the lagoon bottom (as discussed in Sect. 2.1) has been taken into account in the numerical simulations using three different Nikuradse roughness coefficients k_s. Specifically, the values of $k_{s,CN} = 0.3$ m, $k_{s,PO} = 0.1$ m and $k_{s,S} = 0.001$ m have been associated with the presence of Cymodocea nodosa, Posidonia oceanica and sand, respectively. The distribution of the Nikuradse roughness coefficient has been obtained weighting the k_s values reported above according to the percentage of seagrass coverage of each bottom cell, using the formula:

$$k_s = \sqrt{P_S k_{s,S}^2 + P_{CN} k_{s,CN}^2 + P_{PO} k_{s,PO}^2} \tag{14}$$

where P_S, P_{CN} and P_{PO} are the percentages of the cell surface covered with sand, Cymodocea nodosa and Posidonia oceanica, respectively, with $P_S + P_{CN} + P_{PO} = 1$. The seagrass coverage was obtained through remote sensing image analysis [5] and aerial photo interpretation.

Null normal derivatives for velocity and turbulence model variables have been imposed in the northern and southern mouths, while the logarithmic wall-law has been used on the solid boundaries (land and island contours and lagoon bottom). On the free-surface, as discussed above, the wind shear stress has been imposed.

The validation has been achieved comparing the measured and calculated current velocities at the station MS_1 and water levels at MS_2 and MS_3 (see Fig. 1).

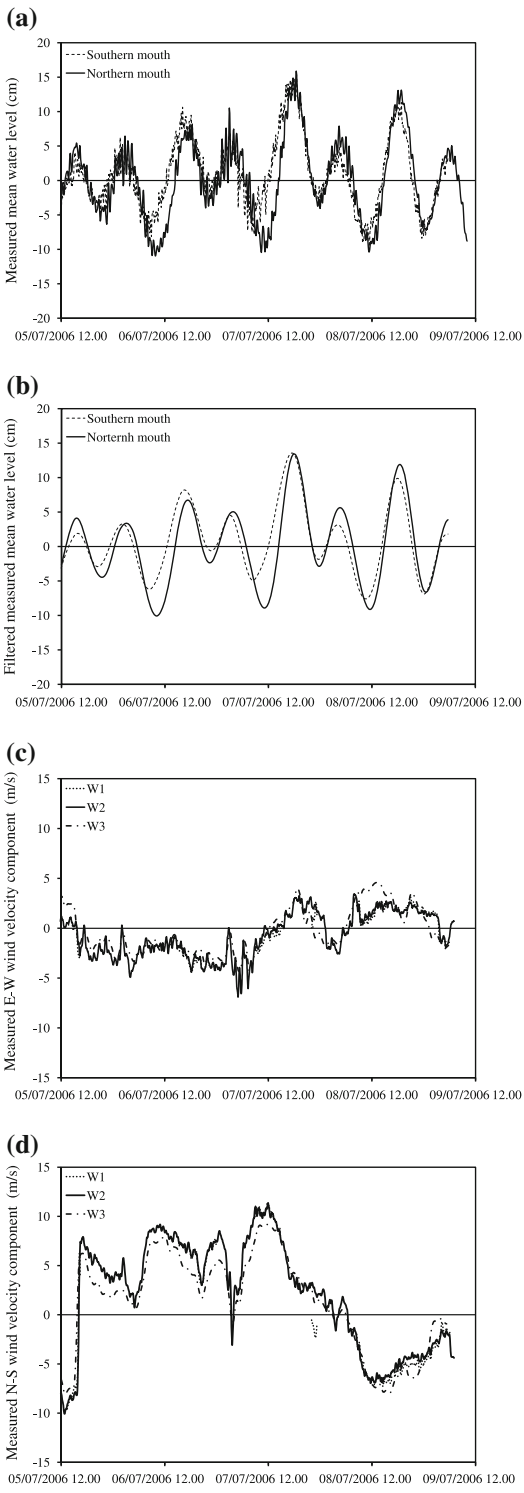

Fig. 3 Measured mean water level in the TS_1 (*continuous line*) and TS_2 (*dashed line*) points and measured wind velocity in the W_1, W_2 and W_3 stations. **a** Measured mean water level; **b** filtered measured mean water level; **c** east-west wind velocity component; **d** north-south wind velocity component

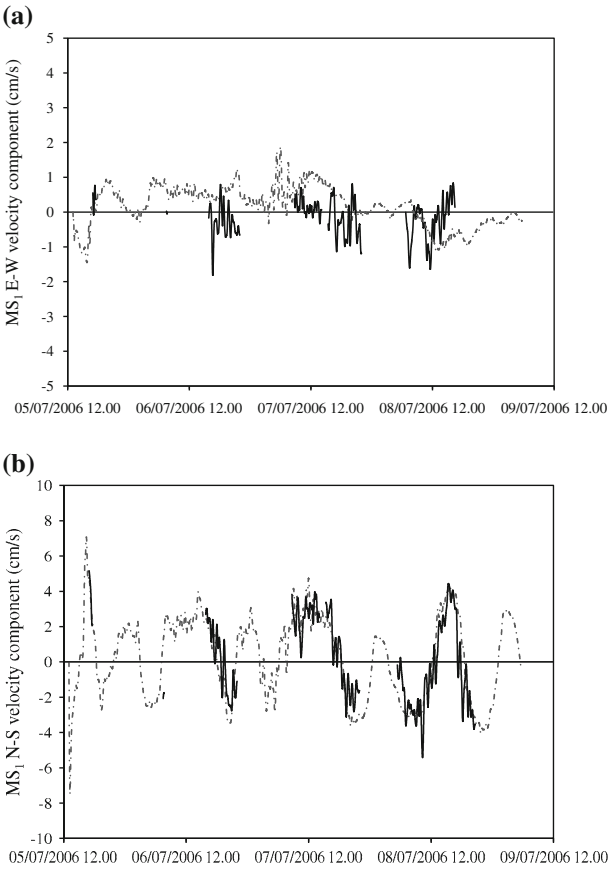

Fig. 4 Comparison between measured and modeled velocity components in the MS_1 station. **a** East-west velocity component; **b** north-south velocity component. *Solid line* measured data; *dot-dashed line* numerical results. Notice the difference in the velocity scale between **a** and **b**

Measured and modeled velocities in the point MS_1, shown in Fig. 4a, b, exhibit a very good agreement in the north-south direction. In the east-west direction, a slightly worse agreement has been found. As discussed in the following, due to the lagoon specific geometry, the eastward velocity component is mostly driven by wind action, while the northward one is influenced by tides. In the simulations the wind spatial inhomogeneity was not accounted for, thus neglecting the wind speed changes occurring close to the coastlines due to the different land and water roughness and temperature. This insufficient description of the wind spatial distribution can be thus the reason for the less satisfactory agreement between measures and numerical results in the east-west direction with respect to the north-south one. Moreover, the comparison between simulated and observed data shows that the numerical results are characterized by lower amplitude oscillations. This behaviour can be attributed as well to the uniform distribution of the wind over the free-surface.

Due to the shallowness and the presence of vegetated bottom, the velocity field is very sensitive to the water level variations. The comparison between the measured and simulated time evolution of the free-surface elevation in the MS_2 and MS_3 points is shown in Fig. 5.

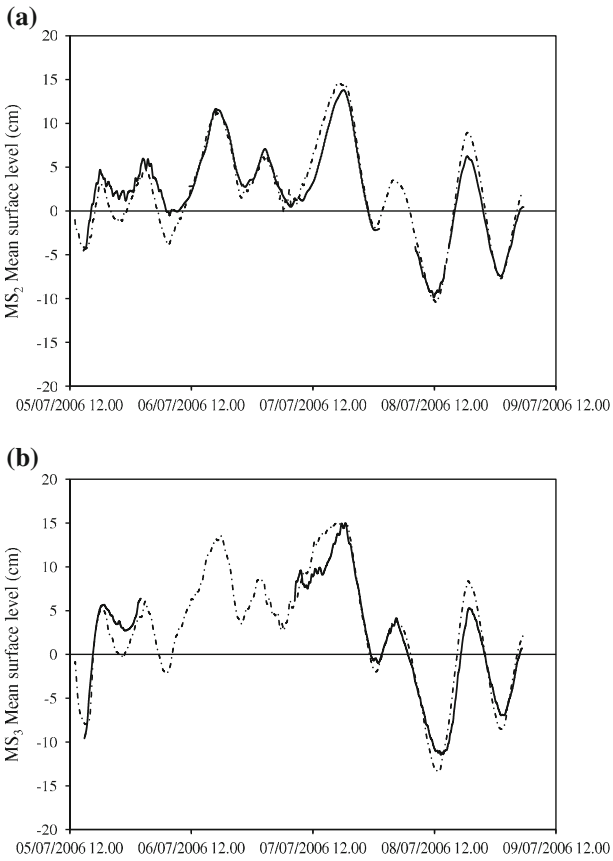

Fig. 5 Comparison between measured and modeled mean surface level in the MS_2 and MS_3 measurement stations. *Solid line* measured data; *dot-dashed line*: numerical results

In both locations a satisfactory agreement is found, confirming that the model is able to reproduce the tidal wave propagation inside the lagoon.

Observed and simulated results reveal on the whole that velocities and free-surface elevations are characterized by tidal oscillations of low frequency and relatively high amplitude and by low amplitude oscillations (with higher frequency) typical of the wind seiche motion. The analysis of the Fourier power spectrum of water levels, not shown here, reveals that tidal oscillations are dominated by the semi-diurnal constituent (12.4 h) with supplementary contribution of the diurnal constituent (24 h). Lower energy peaks characterized by higher frequency and lower amplitude typical of the seiche motion are also observed. Specifically, in the power spectrum of the southern mouth free-surface oscillations, a peak corresponding to a $0.25\,h$ period oscillation was observed. This value is very close to the theoretical value calculated using the Merian's formula $T = 2L/\sqrt{gH}$, with the horizontal and vertical length scales of $L = 3000\,\text{m}$ and $H = 2.5\,\text{m}$, respectively (scales representative of the southern part of the lagoon, characterized by water depth higher than in the northern part).

The results above shown clearly demonstrate that the PANORMUS model is able to predict the hydrodynamic behaviour of the Stagnone lagoon.

4 Comparative analysis of wind and tide effects

The results discussed in the previous section clearly show that the flow field inside the lagoon is driven by the tide and the wind. In order to analyze the relative contributions of these actions on the circulation pattern, two scenarios have been considered. The first (hereafter referred to as TW, Tide-Wind) is the one used in Sect. 3, where both the water level oscillations and the wind action are considered. In the second test case (referred to as TNW, Tide-No-Wind) the effect of the wind distribution over the free-surface has been on the contrary neglected, thus taking into account the tide induced circulation only. In both simulations the same computational domain has been used.

The comparison of the velocity field between the two test cases allows to selectively analyze the effect of the wind and the tide on the lagoon circulation.

A main difference between the velocities obtained in the two test cases is the presence of relatively high frequency velocity oscillations when the wind shear stress is acting, due to the development of seiche motion inside the lagoon. This is clearly evident in Figs. 6 and 7 where horizontal velocity components are shown at different depths and locations as obtained in the two test cases. The values in the figures have been calculated through linear interpolation in the vertical direction of the velocities obtained at the different heights. The spikes at the beginning of the velocity time series in Fig. 6b, d are due to the absence of any spin-up period in the simulations, which started from null velocity.

Specifically, in Fig. 6 the velocity components in the test cases TW and TNW are compared at two different depths, located close to the free-surface and at mid-depth (20 cm and 60 cm below the water level, respectively). The relatively limited difference between the results obtained in the north-south direction (Fig. 6b, d) in the two test cases shows that the circulation is strongly affected by the tidal oscillations. Nevertheless, it can be seen that the non-negligible changes of the flow velocity among the test cases near the free-surface are coherent with the wind direction and intensity (as plotted in Fig. 3c, d). In Fig. 6b, in fact, positive velocities (toward the north) increase in presence of wind blowing from the south (from the 5th to the 7th July), while an increase of mass flow toward the south is observed when it blows from the north (8th July).

On the other hand, at the depth of 60 cm the differences in the north-south direction between the test cases are lower (Fig. 6d). In this case the magnitude of the north-south velocity in presence of wind (TW) is somewhat lower than in TNW with southern wind, while being slightly higher with northern wind.

The wind effects can be isolated analyzing the difference between TW and TNW velocities. On the 6th and 7th may, when the wind blowed from the south, the difference was mostly positive at 20 cm depth and negative at 60 cm depth, while the opposite was obtained on the 8th may, with northern wind. Thus a vertical wind-induced recirculation superimposed to the tidal motion (which is on the contrary almost independent on the depth) is identified.

In the east-west direction (Fig. 6a, c), as discussed in Sect. 3, velocities are quite lower than in the north-south direction. Nevertheless, at 60 cm below the free-surface (Fig. 6c) wind causes the development of eastern flows when it blows from the south and of western flows when it comes from the north. This is due to the morphology of the region close to the point MS_1, as it will be discussed in the following.

In correspondence of the MS_2 point (where the water levels have been measured) the wind produces an increase of the magnitude of the east-west velocity component both near the free-surface and at intermediate depths (Fig. 7a, c). At 60 cm depth the eastward and northward velocity components have about the same values in presence of wind, while north-south velocities are quite higher than east-west ones when tide effects only are considered.

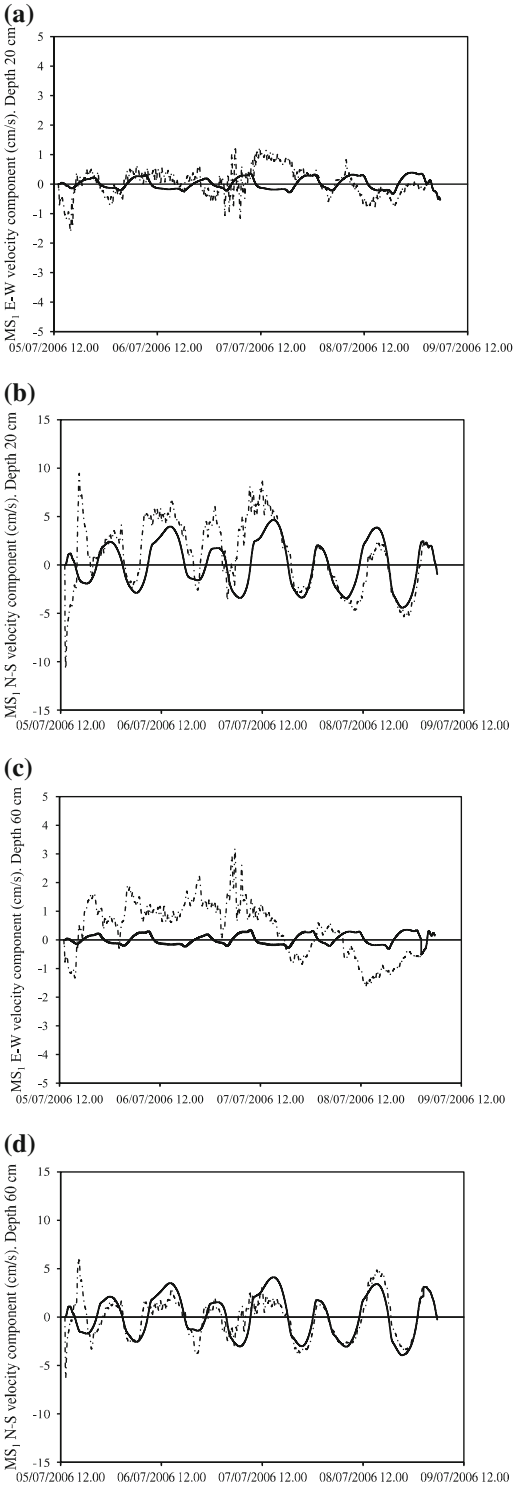

Fig. 6 Comparison between the velocities components obtained with the numerical simulations TW and TNW in correspondence of the MS_1 point. **a** East-west velocity component at 20 cm depth; **b** north-south velocity component at 20 cm depth; **c** east-west velocity component at 60 cm depth; **d** north-south velocity component at 60 cm depth; *dot-dashed line*: TW; *solid line*: TNW. Notice the difference in the velocity scale between **a** and **b**

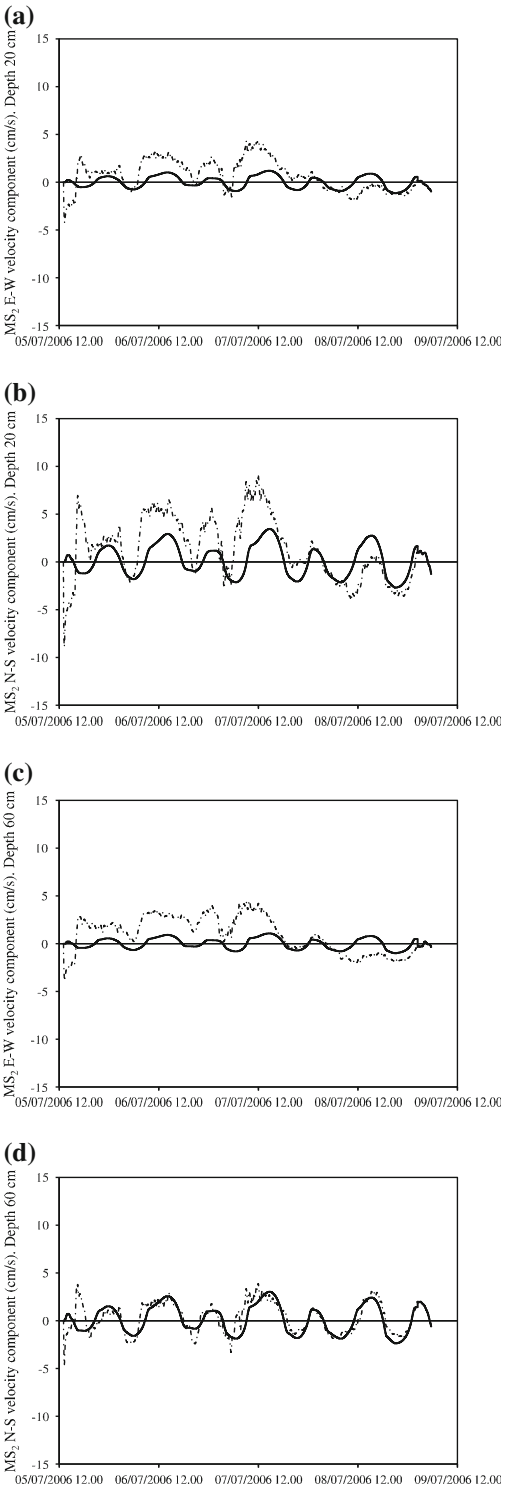

Fig. 7 Comparison between the velocities components obtained with the two numerical simulations TW and TNW in correspondence of the MS_2 point. **a** East-west velocity component at 20 cm depth; **b** north-south velocity component at 20 cm depth; **c** east-west velocity component at 60 cm depth; **d** north-south velocity component at 60 cm depth. *Dot-dashed line*: TW; *solid line*: TNW

The vertical wind-induced recirculation discussed above is clearly evident in Fig. 8, close to the MS_2 measurement station, located near the coast of Isola Grande. In the figure the velocity flow fields at the depths of 20 and 60 cm below the free-surface, for the test cases TW and TNW, are plotted, as obtained on midday of the 6-th July, with a wind from south-east. The recirculation explains the increase of the eastward velocity component observed in Figs. 6c and 7c in presence of wind. On the other hand, the comparison between Fig. 8c, d shows, coherently with the results observed in Figs. 6b and 7b, that near the free-surface the wind enhances the circulation pattern driven by the tidal force. Specifically, wind action enhances free-surface movements, causing the development of pressure gradients that are responsible for the recirculation phenomena below the free-surface shown in Fig. 8a.

An analogous pattern can be observed in Fig. 9, where the velocity fields obtained at midday of July 8 are analyzed. In this case the wind direction is south-east. At the intermediate depth, coherently with the observation of Fig. 8a, in the TW case the wind produces large recirculations (Fig. 9a), that are not present when the wind is neglected (TNW) (Fig. 9b). In this case, in fact, the current is clearly directed northward (Fig. 9b, d), without giving rise to recirculation phenomena, as it is well known in the oceanographic literature on tidal flows. The tidal waves thus enter inside the lagoon from the southern mouth and propagate toward the northern one with smaller velocities than those observed when the wind is blowing. Moreover, the velocities at 20 and 60 cm depths are quite similar. On the contrary, when the wind is acting, coherently with the observed data, a vigorous current with southward velocity all over the lagoon is observed (see Fig. 9c).

The circulation induced by the wind is clearly shown in Fig. 10. In the figure the velocity flow field in the east-west vertical cross-section in correspondence of the MS_2 point is plotted on midday of July 8 for the two test cases TW and TNW. The comparison between Fig. 10a, b, where the north-south velocity component in the cross section S_1-S_1, specified in Fig. 1, is plotted, shows that the wind strongly affect the vertical distribution of horizontal currents, thus playing a fundamental role in the transport of pollutants and suspended material. Furthermore, the results shown above clearly demonstrate the need to use 3D numerical models even in very shallow waters, at least when wind effects have to be taken into account.

5 Conclusions

A 3D numerical model has been used to analyze the hydrodynamics of the Stagnone di Marsala lagoon, located in the north-western part of Sicily (Italy). The numerical results have been compared with field data. The comparison showed the ability of the PANORMUS numerical model to reproduce the hydrodynamics inside the lagoon. The model adequately reproduces the free-surface elevation and the current generated by the Mediterranean Sea tide and by the wind acting on the lagoon. The seiche motion is well reproduced too.

The comparison between numerical results obtained forcing the flow field with wind and tides (case TW) and tides only (case TNW) shows that, even if the tidal force mainly drives the current in the north-south direction, the wind strongly modifies the circulation modulated by the tide. Near the free-surface, in fact, the wind action enhances the current imposed by the tidal force and sometimes is able to invert the direction of the flow field. Below the free-surface the wind generates wide recirculation regions, increasing the water mixing.

Even if the model is able to simulate the hydrodynamic flow field inside the lagoon, a certain level of disagreement in the east-west direction between measured and simulated velocities was found. Due to the importance of the wind field on the circulation pattern, in further simulations a more accurate spatial distribution of the wind will be taken into account

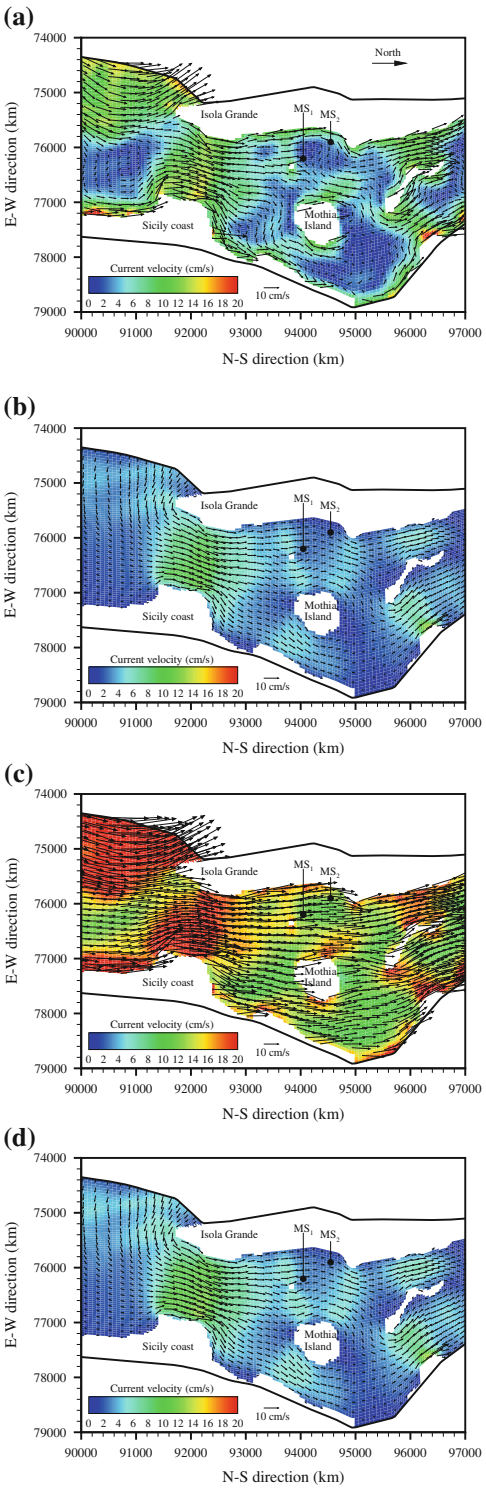

Fig. 8 Circulation pattern at 20 and 60 cm depths, at midday of 6th July. **a** TW 60 cm depth; **b** TNW 60 cm depth; **c** TW 20 cm depth; **d** TNW 20 cm depth. Wind direction is north-west

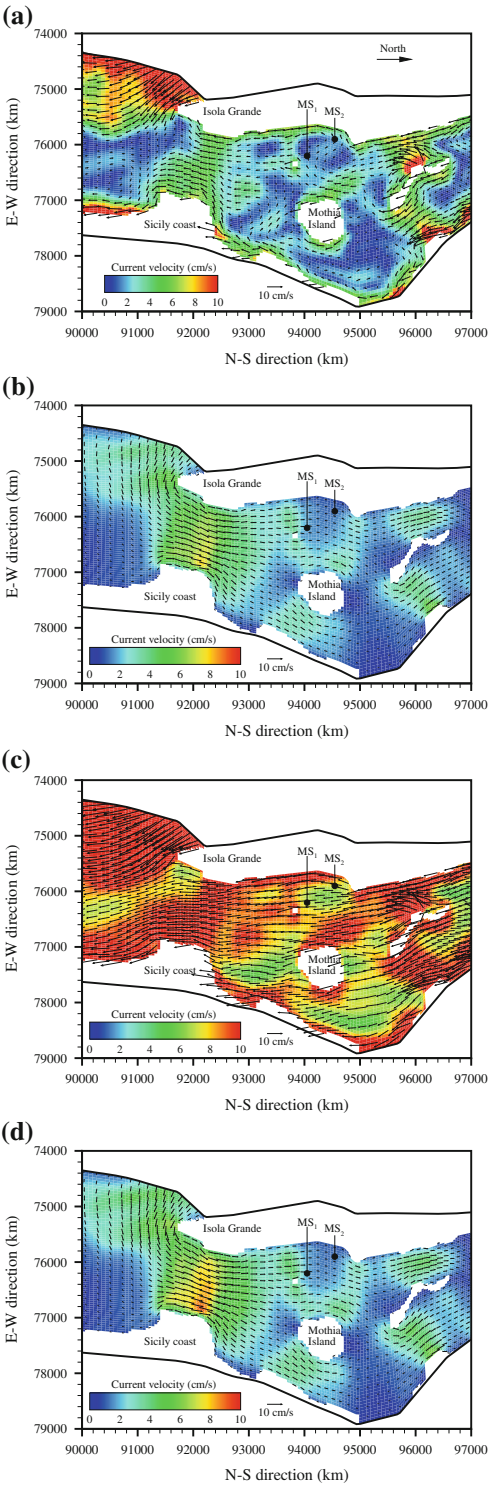

Fig. 9 Circulation pattern at 20 and 60 cm depths, at midday of 8th July. **a** TW 60 cm depth; **b** TNW 60 cm depth; **c** TW 20 cm depth; **d** TNW 20 cm depth. Wind direction is south-east

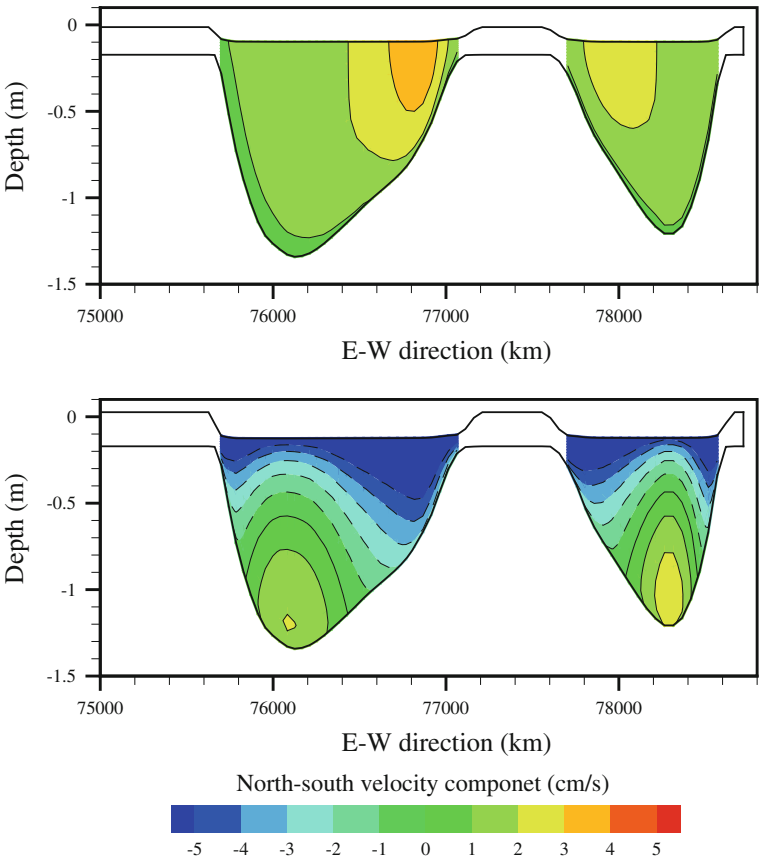

Fig. 10 North–south velocity flow field in the east-west vertical plane located in correspondence of the MS_2 point on midday of July 8. The cross section is indicated in Fig. 1 with the symbol $S_1 - S_1$. The cross section is indicated in f. **a** TNW; **b** TW. Wind direction is south-east. *Dashed line* negative values of the velocities (Southward direction)

as generated by the different roughness of land and water surface. These inhomogeneities are responsible for the formation of an Internal Boundary Layer (IBL) in the lowermost part of the Atmospheric Boundary Layer, causing a wind dependence on the fetch, to be taken into account to better describe flow fields [12] close to coastlines.

References

1. Alpar B, Yuce H (1996) Sea-level variations in the eastern coasts of the Aegean Sea. Estuar Coast Shelf Sci 42:509–521
2. Babu MT, Vethamony P, Desa E (2005) Modelling tide-driven currents and residual eddies in the Gulf of Kachchh and their seasonal variability: a marine environmental planning perspective. Ecol Model 184:299–312
3. Balas L, Ozhan E (2002) Three-dimensional modelling of stratified coastal waters. Estuar Coast Shelf Sci 54:75–87
4. Borthwick AGL, Cruz-Leon S, Jozsa J (2001) Adaptive quadtree model of shallow-flow hydrodynamics. J Hydraul Res 39(4):413–424

5. Calvo S, Ciraolo G, La Loggia G (2003) Monitoring *Posidonia oceanica* meadows in a mediterranean coastal lagoon (Stagnone, Italy) by means of neural network and isodata classification methods. Int J Remote Sens 24(13):2703–2716
6. Cioffi F, Gallerano F, Napoli E (2005) Three-dimensional numerical simulation of wind driven flows in closed channels and basins. J Hydraul Res 43(3):290–301
7. De Marchis M, Napoli E (2008) The effect of geometrical parameters on the discharge capacity of meandering compound channels. Adv Water Resour 31:1662–1673
8. Ferrarin C, Umgiesser G (2005) Hydrodynamic modeling of a coastal lagoon: The Cabras lagoon in Sardinia, Italy. Ecol Model 188:340–357
9. Ferrarin C, Umgiesser G, Bajo B, Bellafiore D, De Pascalis F, Ghezzo M, Mattassi G, Scroccaro I (2010) Hydraulic zonation of the lagoons of Marano and Grado, Italy. A modelling approach. Estuar Coast Shelf Sci. doi:10.1016/j.ecss.2010.02.012
10. Grifoll M, Fontan A, Ferrer L, Mader J, Gonzalez M, Espino M (2009) 3D hydrodynamic characterization of a meso-tidal harbour: the case of Bilbao (northern Spain). Coast Eng 56:907–918
11. Iglesias G, Carballo C, Castro A (2008) Baroclinic modelling and analysis of tide- and wind-induced circulation in the Ria de Muros (NW Spain). J Marine Syst 74:475–484
12. Jozsa J, Milici B, Napoli E (2007) Numerical simulation of internal boundary-layer development and comparison with atmospheric data. Bound-Lay Meteorol 123(1):159–175
13. Kramer T, Jozsa J (2005) An adaptively refined, finite-volume model of wind-induced currents in lake neusiedl. Period Polytech Civ Eng 49(2):111–136
14. Kramer T, Jozsa J (2007) Solution-adaptivity in modelling complex shallow flows. Comput Fluids 36:562–577
15. Launder BE, Spalding DB (1974) The numerical computation of turbulent flows. Comput Method Appl Meach 3:269–289
16. Lipari G, Napoli E (2008) The impacts of the ale and hydrostatic-pressure approaches on the energy budget of unsteady free-surface flows. Comput Fluids 37(6):656–673
17. MacCready P, Banas NS, Hickey BM, Dever EP, Liu Y (2009) A model study of tide- and wind-induced mixing in the Columbia River Estuary and plume. Cont Shelf Res 29:278–291
18. Marinov D, Norro A, Zaldivar JM (2006) Application of COHERENS model for hydrodynamic investigation of Sacca di Goro coastal lagoon (Italian Adriatic Sea shore). Ecol Model 193:52–68
19. Napoli E (2011) PANORMUS User's manual. University of Palermo, Palermo, Italy, pp 1–74. www.panormus3d.org
20. Napoli E, Armenio V, De Marchis M (2008) The effect of the slope of irregularly distributed roughness elements on turbulent wall-bounded flows. J Fluid Mech 613:385–394
21. Niedda M, Greppi M (2007) Tidal, seiche and wind dynamics in a small lagoon in the Mediterranean Sea Estuarine. Estuar Coast Shelf Sci 74:21–30
22. Rhie CM, Chow WL (1983) Numerical study of the turbulent flow past an airfoil with trailing edge separation. AIAA J 21(11):1525–1532
23. Roman F, Napoli E, Milici B, Armenio V (2009) An improved immersed boundary method for curvilinear grids. Comput Fluids 38:1510–1527
24. Roman F, Stipcich G, Armenio V, Inghilesi R, Corsini S (2010) Large eddy simulation of mixing in coastal areas. Int J Heat Fluid Flow 31(3):327–341
25. Shulman I, Wua CR, Lewis JK, Paduan JD, Rosenfeld LK, Kindled JC, Ramp SR, Collins CA (2002) High resolution modeling and data assimilation in the Monterey Bay area. Cont Shelf Res 22(8):1129–1151
26. Suursaar U, Kullas T, Otsmann M (2002) A model study of the sea level variations in the Gulf of Riga and the Vainameri Sea. Cont Shelf Res 22:2001–2019
27. Wu J (1982) Wind-stress coefficients over sea surface from breeze to hurricane. J Geophys Res 87:9704–9706